Supporting Information

Enhanced Electrochemical CO_2-to-Ethylene Conversion through Second-Shell Coordination on Cu Single-Atom Catalyst

Yi Shen[a,b]*, Yongliang Pan[a], Huanyong Xiao[a], Haizhong Zhang[a], Chao Zhu[a]*, Qile Fang[c], Yungui Li[d], Lun Lu[e], Liqun Ye[f], Shuang Song[a]

[a] College of Environment, Zhejiang University of Technology, Hangzhou, 310032, P. R. China;

[b] Shaoxing Research Institute, Zhejing University of Technology, Shaoxing, 312000, P. R. China;

[c] Advanced Institute of Natural Sciences, Beijing Normal University at Zhuhai, Zhuhai, 519087, P. R. China;

[d] Sichuan Provincial Sci-Tech Cooperation Base of Low-cost Wastewater Treatment Technology, Department of Environmental Engineering, Southwest University of Science and Technology, Mianyang, 621010, P. R. China;

[e] State Environmental Protection Key Laboratory of Environmental Pollution Health Risk Assessment, South China Institute of Environmental Sciences, Ministry of Ecology and Environment, Guangzhou, 510655, P. R. China.

[f] College of Materials and Chemical Engineering, Key Laboratory of Inorganic Nonmetallic Crystalline and Energy Conversion Materials, China Three Gorges University, Yichang, 443002, P. R. China.

*Corresponding Author Prof. Yi Shen, Chao Zhu. Email: shenyi@zjut.edu.cn, zhuchao@zjut.edu.cn. Fax: +86-571-88320276; Tel: +86-571-88320726.

Experimental Section

Synthesis of g-C_3N_4

The g-C_3N_4 was prepared following a typical thermal polymerization procedure. Briefly, 15 g of urea was put into a covered crucible and then heated to 600 °C at a ramp rate of 5 °C/min in a muffle furnace. It was maintained at this temperature for an additional 2 h. After being cooled down to room temperature, the resultant powders (about 500 mg) were ultrasonicated with deionized water, collected by filtration, and finally dried under vacuum at 60 °C.

Synthesis of heteroatom-doped g-C_3N_4

Heteroatom-doped g-C_3N_4 was synthesized through a typical procedure. Take C_3N_4-S for example, pristine g-C_3N_4 (0.2 g) and sulfur powder (0.01 g) were ground in an agate mortar for 30 min. The mixture was then pressed in a tube furnace and reacted at 550 °C for 2 h with a heating rate of 2 °C/min and the Ar gas (purity > 99.999%) flow of 0.1 L/min. The end of the tube furnace was connected to a gas bottle containing ethanol in case of a trace amount of volatile gas. After cooling to room temperature, the resulting powder was filtered and washed successively with deionized water and alcohol, and dried in a vacuum at 60 ℃. The C_3N_4-B and C_3N_4-P samples were synthesized by the same method as above, except that the sulfur powder was replaced by the boron powder and sodium hypophosphite ($NaH_2PO_2 \cdot H_2O$), respectively.

Preparation of Cu-C_3N_4-X

In a typical synthesis, an aqueous suspension of C_3N_4-S (approximately 2.5 $mg \cdot mL^{-1}$) was first prepared by dispersing 150mg C_3N_4-S into 60 mL deionized water with sonication and was then kept stirring continuously. Preparation of copper chloride aqueous suspension, dissolving 46 mg Copric chloride dihydrate (approximately 1.15 $mg \cdot mL^{-1}$) into 40 mL deionized water with sonication. Then, added copper chloride aqueous suspension dropwise to C_3N_4-S aqueous suspension and kept stirring for 24 h to form a homogeneous solution. After the impregnation step, the resulting homogeneous solution was filtered and washed successively with alcohol and deionized water, and dried in a vacuum at 60 °C. To prepare the Cu-C_3N_4-S sample, the obtained

impregnated sample was placed in the tube furnace and annealed at 550 °C for 2 h with the heating rate of 2 °C/min and the Ar atmosphere. The Cu-C_3N_4-B and Cu-C_3N_4-P samples were synthesized by the same method as above, except that the C_3N_4-S were replaced by C_3N_4-B and C_3N_4-P, respectively.

Preparation of $Cu_{x\%}$-C_3N_4-S

The $Cu_{x\%}$-C_3N_4-S was obtained by continuing to follow the preparation steps of C_3N_4-S based on the Cu-C_3N_4-S prepared in the previous steps. But the proportion of Cu element into C_3N_4-S changed to 2%, 5%, and 15%. To facilitate the discussion, $Cu_{x\%}$-C_3N_4-S were named according to the ratio of Cu element to C_3N_4-S in the catalyst.

Characterization of Cu-C_3N_4-S, Cu-C_3N_4-B, Cu-C_3N_4-P, Cu-C_3N_4 and C_3N_4

Field emission scanning electron microscopy (FESEM) was utilized to show the structure of the catalysts on the Regulus8100 and the accelerating voltage was set as 15 kV. Furthermore, high-resolution transmission electron microscopy (HRTEM) and energy dispersive X-Ray (EDX) elemental mapping were used to characterize the morphologies of the catalysts and spatial distribution of elements on a JEM-F200 with an accelerating voltage of 300 kV. Powder X-ray diffraction (XRD) measurements were performed on a Smart Lab SE diffractometer using Cu targets (tube voltage: 40 kV, current: 30 mA). The functional group structure was measured by Fourier transform infrared spectroscopy (FT-IR). Inductively coupled plasma optical emission spectrometer (ICP-OES) results were obtained by assays from Agilent 5110 instruments. High-angle annular dark-field scanning transmission electron microscopy (HAADF-STEM) was performed using a state-of-the-art transmission electron microscope equiped with double (image and probe) spherical aberration (Cs) correctors (Thermo Scientific Spectra 300). X-ray photoelectron spectroscopy (XPS) spectra were collected with an ESCALAB 250Xi instrument using an Al Kα X-ray as an excitation source. In situ Raman was conducted on a HORIBA LabRAM HR Evolution Raman spectrometer with a 532 nm solid laser as an excitation source. The measurements were carried out in a home-made flow cell with a quartz window to detect the signal from cathode GDE. The Cu K-edge X-ray absorption near edge structure (XANES)

measurements was performed on a laboratory device (easyXAFS300, easyXAFS LLC), which was based on Rowland circle geometries with spherically bent crystal analyzers (SBCA) and operated using an Ag X-ray tube source and a silicon drift detector (AXAS-M1, KETEK GmbH).

CO_2 reduction reaction measurements

Electrochemical measurements were conducted using a CHI760E electrochemical station (China) within a reactor featuring two electrode chambers separated by an ion exchange membrane, equipped with three electrodes. The cathode and anode electrodes consisted of carbon paper (2 cm × 2 cm) with catalyst and nickel foam (2 cm ×2 cm), respectively. A reference electrode of Ag/AgCl (3.5 M KCl) was employed. The catalyst ink, fully dispersed, was prepared by ultrasonically vibrating a mixture of catalyst (3 mg), absolute ethanol (300 μL, YongDa, China), and Nafion (50 μL, HeSen, China) for 30 minutes. Cathode electrodes were then fabricated by evenly spreading 100 μL of the catalyst ink onto carbon paper and drying it overnight under vacuum. The electrode potentials were converted from the reversible hydrogen electrode (RHE) reference:

$$E(\text{vs. RHE}) = E(\text{vs. Ag/AgCl}) + 0.0591 \times \text{pH} + 0.197$$

To assess the Faradaic efficiencies (FEs) of the CO_2RR products, chronoamperometry was conducted for 8000 s at a range of potentials (typically, at -0.8, -1.0, -1.1, -1.2, -1.3, -1.4 V). Gas products were analyzed every 30-minute intervals during the CO_2RR and after the reaction by Gas Chromatography (GC), and the average value of the whole process was adopted. Liquid products were analyzed after reaction by ^{1}H nuclear magnetic resonance (NMR) spectroscopy. Linear sweep voltammetry (LSV) was carried out from 1.6 V to -1.4 V vs. RHE in CO_2-saturated 0.1 M $KHCO_3$ to evaluate CO_2RR activity. Stability tests were conducted in a 0.1 M $KHCO_2$ electrolyte solution saturated with CO_2 at -0.9 V vs. RHE for 1440 min. During the stability test, CO_2 was kept purging into the cathodic room at 10 sccm with stirring at 500 rpm. C_2H_4 production was monitored by GC every 30 min. Cyclic voltammograms (CV) measurements were conducted at various scan rates (100, 130, 160, 190, 210 $mV \cdot s^{-1}$) within the potential windows of open circuit voltage (± 0.3 V) (vs. Ag/AgCl).

By plotting the Δj (the difference between cathodic and anodic current density) against the scan rate at open circuit voltage (vs Ag/AgCl). The double layer capacitance (C_{dl}) could be obtained from half of the corresponding slope value.

Faraday efficiency (FE) calculation formula for a gas product was as follows:

$$FE_g = \frac{Q_g}{Q_{total}} \times 100\% = \frac{\frac{v}{60\ s/min} \times \frac{y}{24.5\ L/mol} \times n \times F}{j_{average}} \times 100\%$$

where v is the flow rate of CO_2 gas, controlled by the gas flow meter at 10 sccm; y is the volume percentage of the target component in the exhaust gas obtained by gas chromatography; for gas phase reduction products H_2, CO, CH_4, and C_2H_4, n is 2, 2, 8 and 12 respectively; F is Faraday constant (F = 96485.3 C mol^{-1}); $j_{average}$ is the average current.

Computation details

DFT calculations were performed using the Vienna Ab-initio Simulation Package (VASP).[1, 2] The Perdew-Burke-Ernzerhof (PBE) functional within the generalized gradient approximation (GGA) method was employed to account for exchange-correlation effects.[3, 4] Core-valence interactions were treated using the projected augmented wave (PAW) method.[5] A plane wave energy cutoff of 450 eV was set, and a 3×3×1 Monkhorst-Pack k-point grid was utilized for Brillouin zone sampling. To prevent periodic interactions, a vacuum space of 15 Å above the surfaces was adopted. The self-consistent calculations applied a convergence energy threshold of 10-5 eV. The equilibrium geometries and lattice constants were optimized with maximum stress on each atom within 0.02 eV $Å^{-1}$. Isosurface level of charge density difference of Cu-C_3N_4-S was set at 0.01 e $Å^{-3}$. Density of states of Cu-C_3N_4-S, Cu-C_3N_4-B, Cu-C_3N_4-P, Cu-C_3N_4-S-CO, Cu-C_3N_4-B-CO, and Cu-C_3N_4-P-CO were both obtained by vaspkit interface.

In Gibbs free energy calculation,the elementary steps of C-C coupling reaction were described as:

*CO-CO → *COCO

In reaction pathways, the sign of "*" represents the bare surface. The sign of "-" represents the situation of intermediates which adsorbed on surface before C-C coupling. Besides, the Kelvin temperature T was set at 298.15K. Ezpe and TS were both obtained by vaspkit interface. pH value was set at 8 to simulate the weakly alkaline media medium.

The Gibbs free energy change (ΔG) of each step is determined using the formula:

$$\Delta G = \Delta E + \Delta ZPE - T\Delta S$$

where ΔE represents the electronic energy difference directly obtained from DFT calculations, ΔZPE is the zero-point energy difference, T is the room temperature (298.15 K) and ΔS is the entropy change. The ΔZPE can be obtained following frequency calculations[6]:

$$\mathrm{ZPE} = \frac{1}{2}\sum hvi$$

Additionally, the TS values of adsorbed species are calculated according to the vibrational frequencies[7]:

$$TS = k_B T \left[\sum_k ln(\frac{1}{1-e^{-hv/k_B T}}) + \sum_k \frac{hv}{k_B T} \frac{1}{(e^{hv/k_B T}-1)} + 1 \right]$$

159

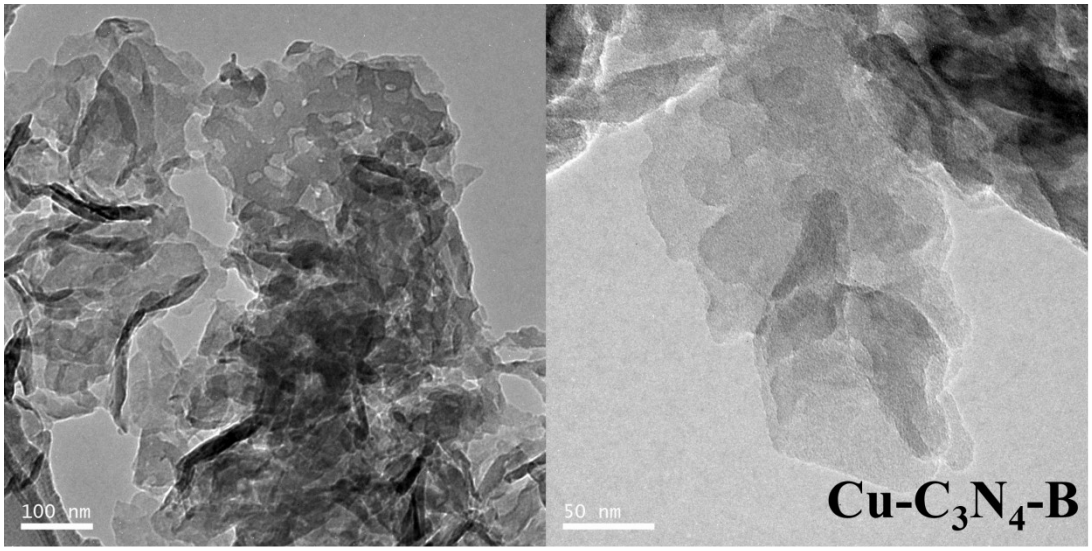

160

161 **Fig. S1.** FE-SEM and HR-TEM images of Cu-C_3N_4-B.

162

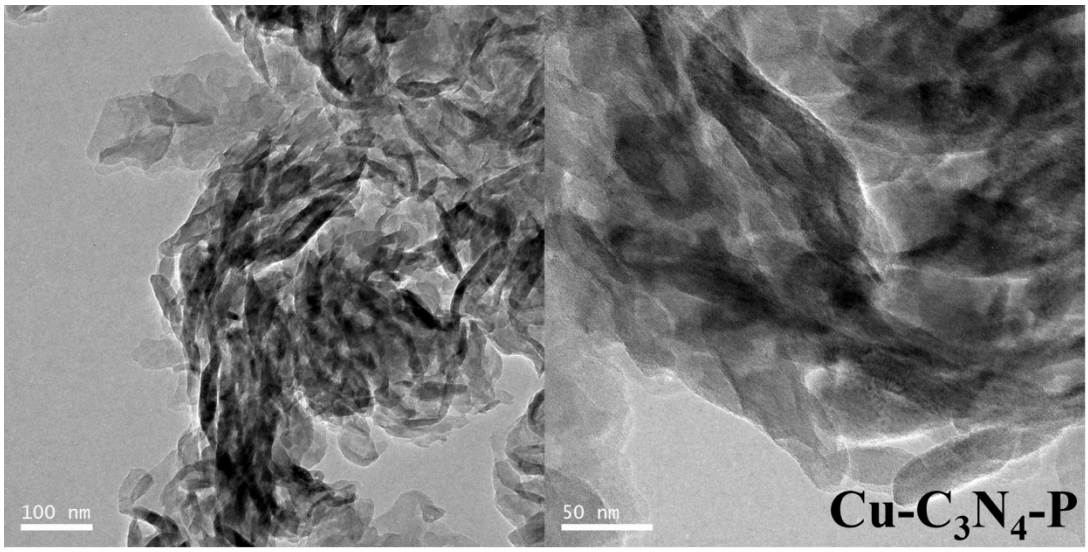

Fig. S2. FE-SEM and HR-TEM images of Cu-C_3N_4-P.

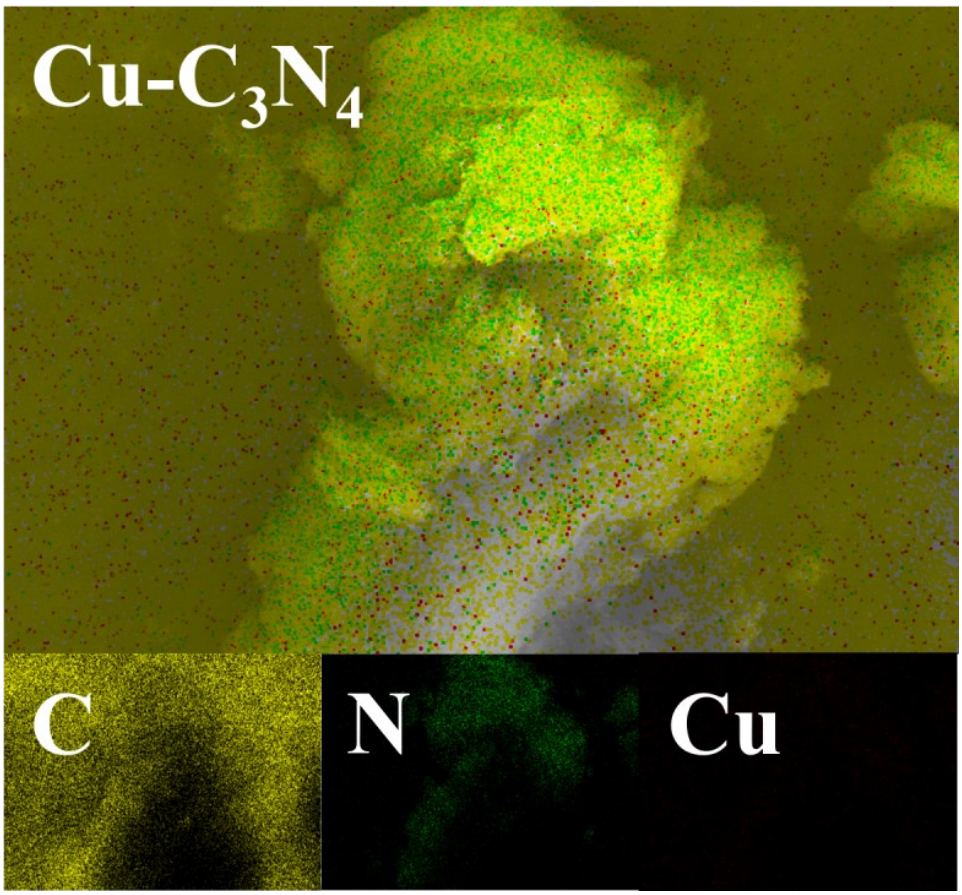

Fig. S3. HR-TEM and corresponding EDXs mapping images of Cu-C_3N_4.

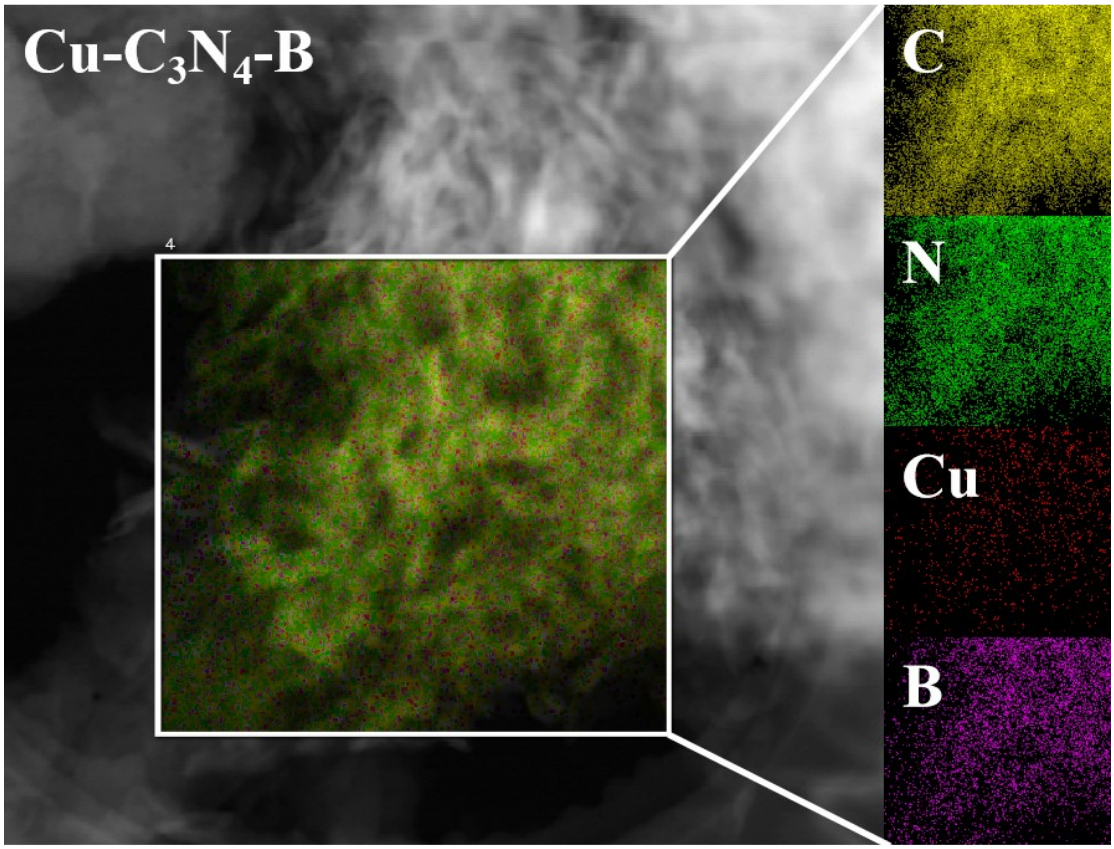

Fig. S4. HR-TEM and corresponding EDXs mapping images of Cu-C_3N_4-B.

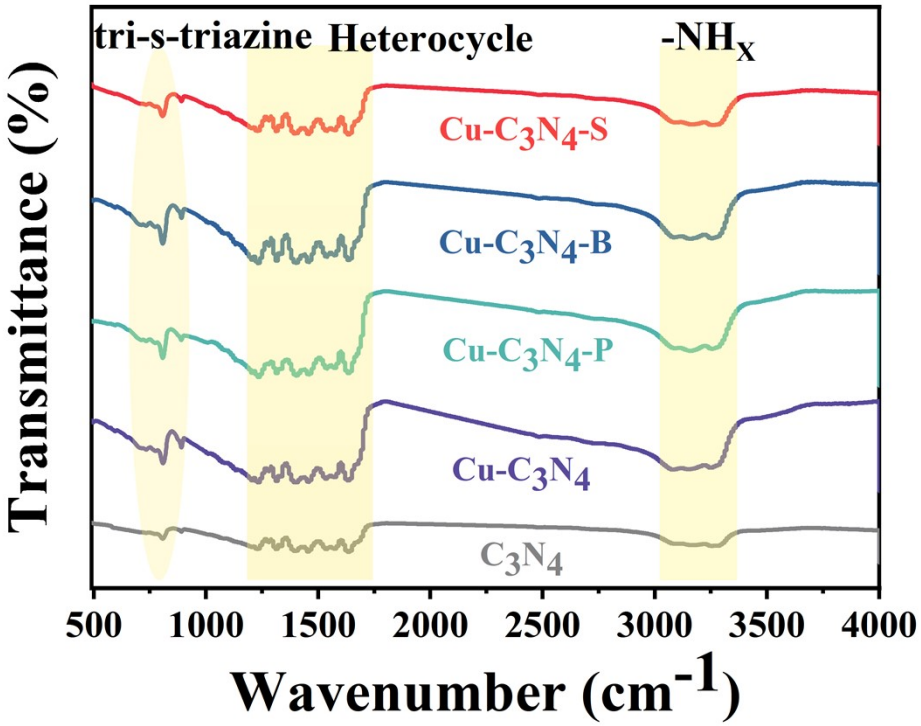

172

173 **Fig. S5.** FT-IR spectra of Cu-C_3N_4, C_3N_4 and Cu-C_3N_4-HA.

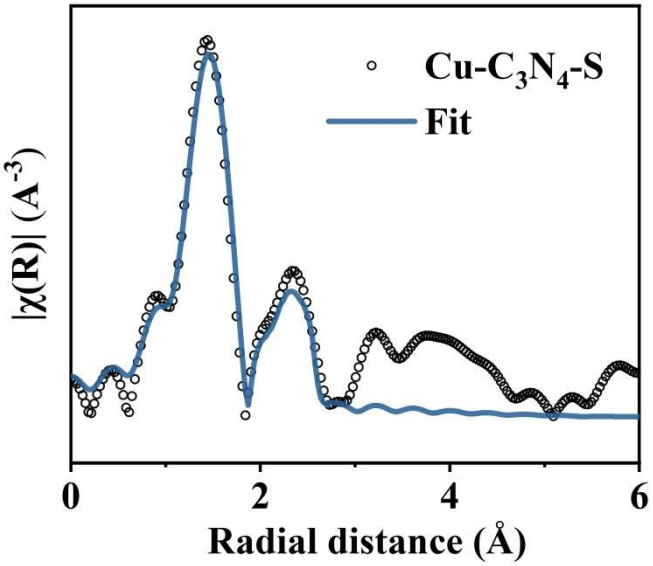

Fig. S6. Cu K-edge EXAFS fitting curves of Cu-C_3N_4-S.

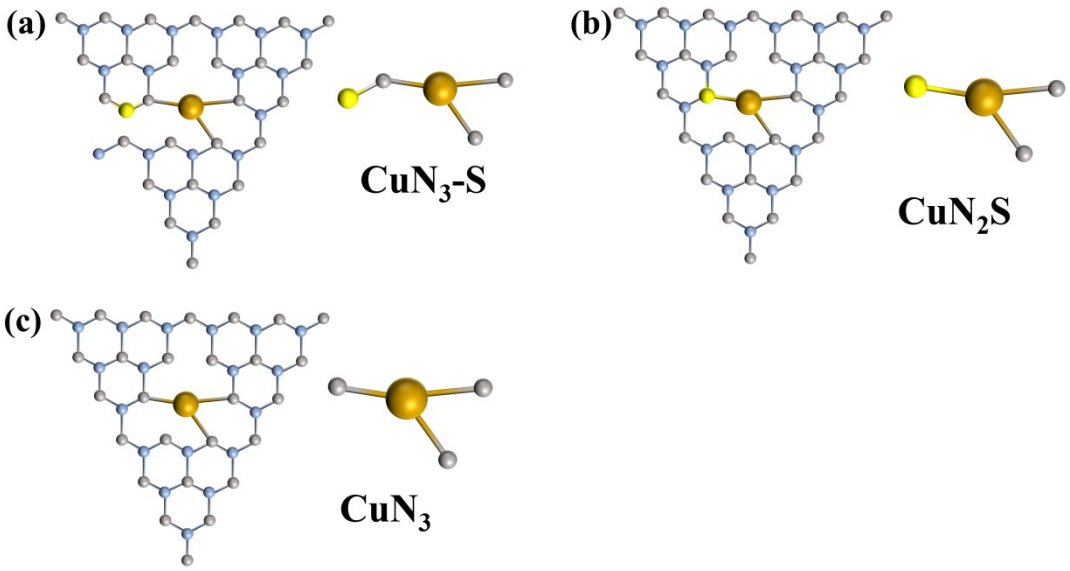

Fig. S7. The DFT calculation configurations of (a) CuN_3-S, (b) CuN_2S, and (c) CuN_3 moieties embedded in a graphene sheet. Color scheme: grey for N, yellow for S, blue for C, and golden for Cu.

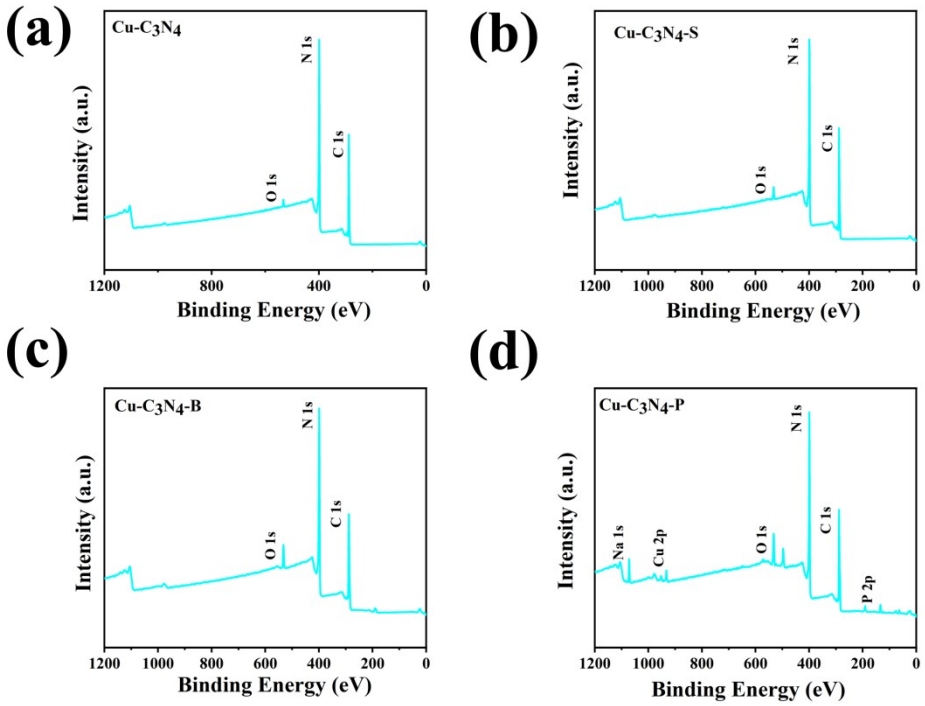

Fig. S8. (a-d) XPS spectra of Cu-C_3N_4 and Cu-C_3N_4-HA.

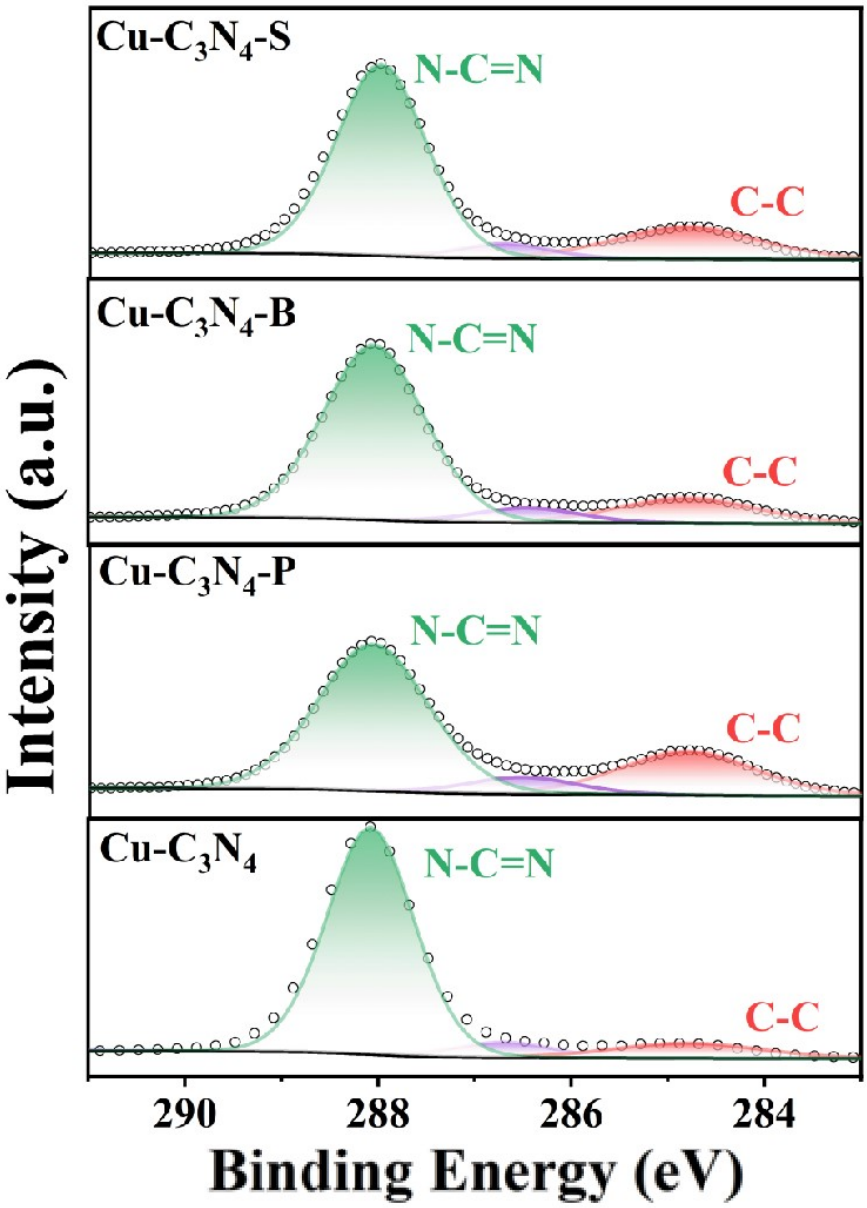

Fig. S9. High-resolution C 1s spectra of Cu-C_3N_4 and Cu-C_3N_4-HA.

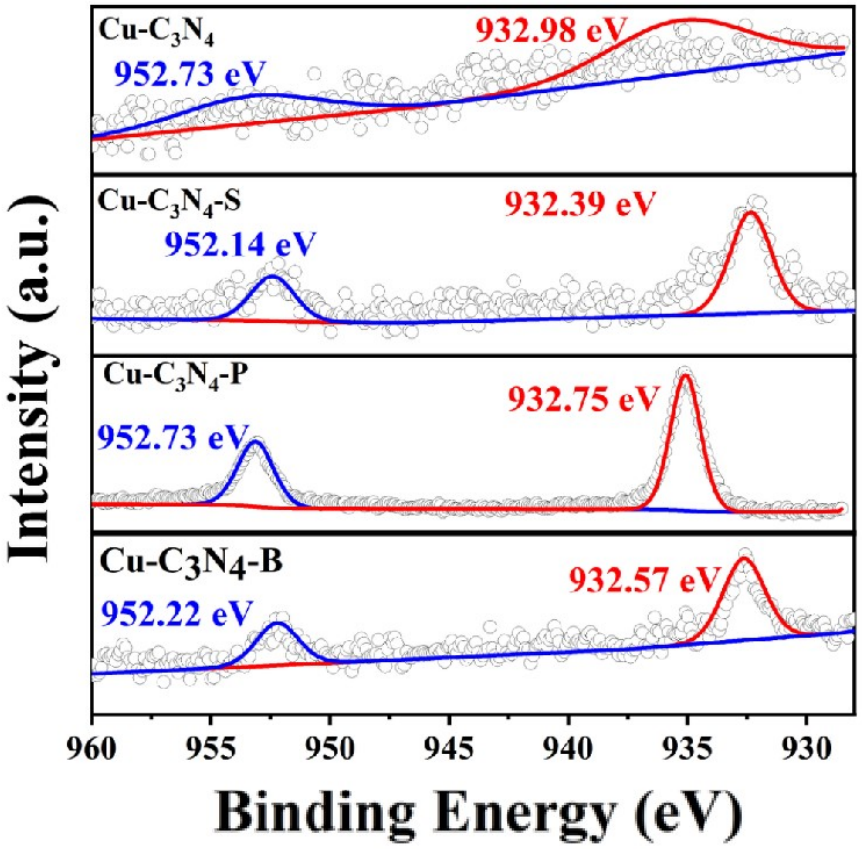

Fig. S10. High-resolution Cu 2p spectra of Cu-C_3N_4 and Cu-C_3N_4-HA.

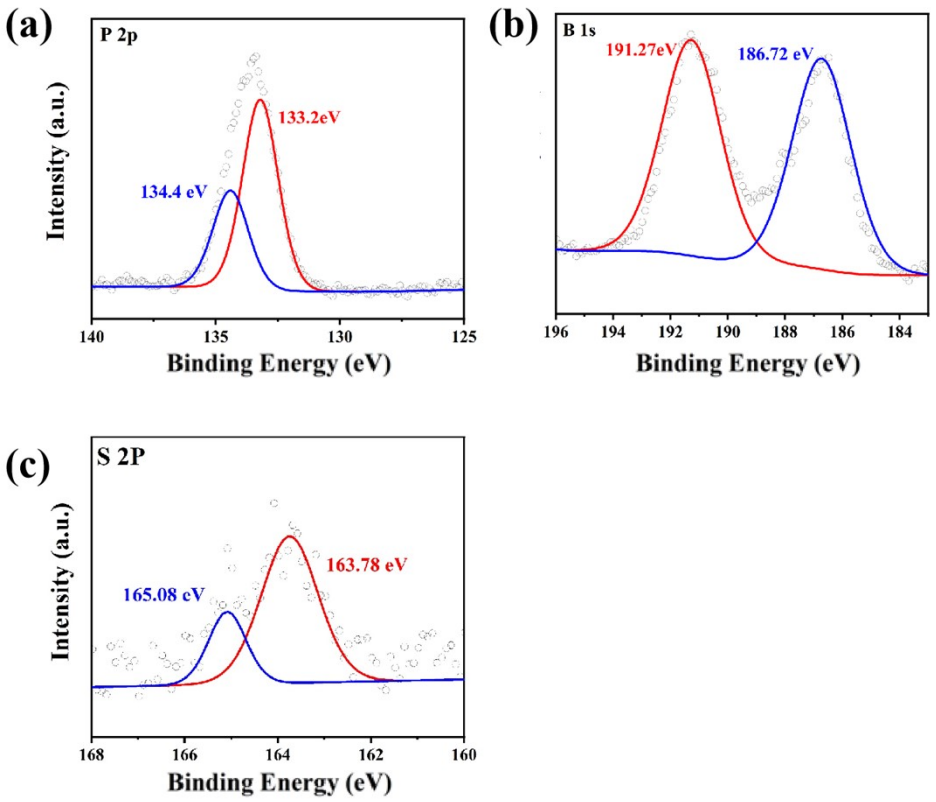

Fig. S11. (a) High-resolution P 2p spectra of Cu-C_3N_4-P. (b) High-resolution B 1s spectra of Cu-C_3N_4-B. (c) High-resolution S 2p spectra of Cu-C_3N_4-S.

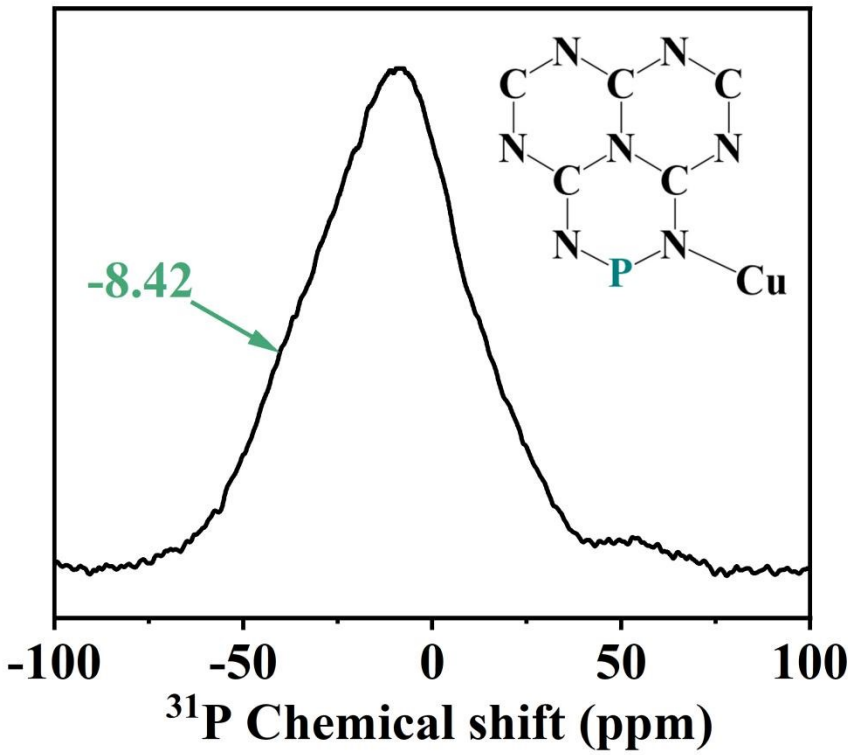

Fig. S12. ^{31}P solid-state NMR spectrum of Cu-C_3N_4-P.

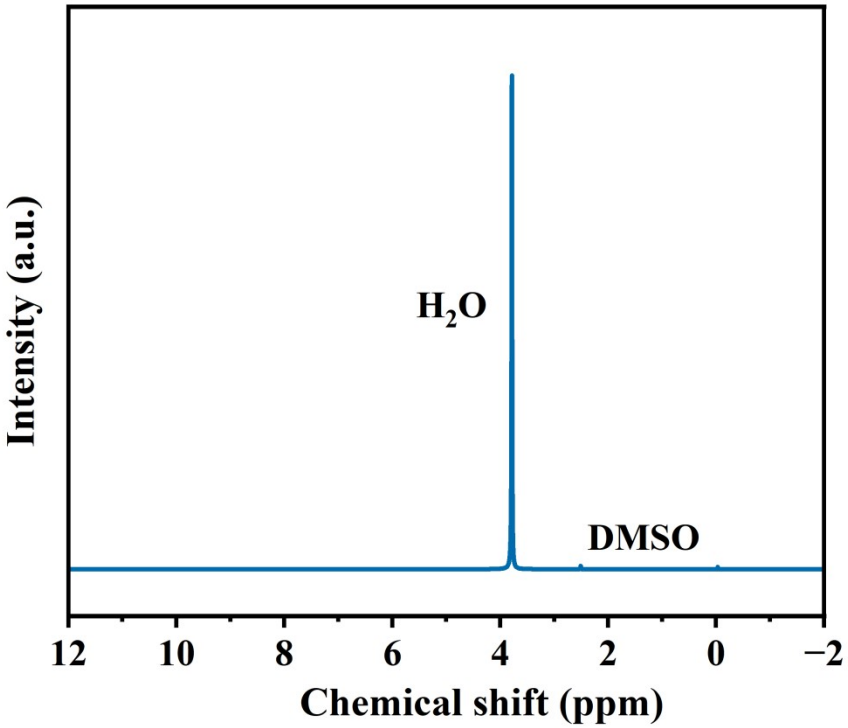

Fig. S13. ^{1}H NMR results of Cu-C_3N_4-HA after 2 h continuous CO_2RR.

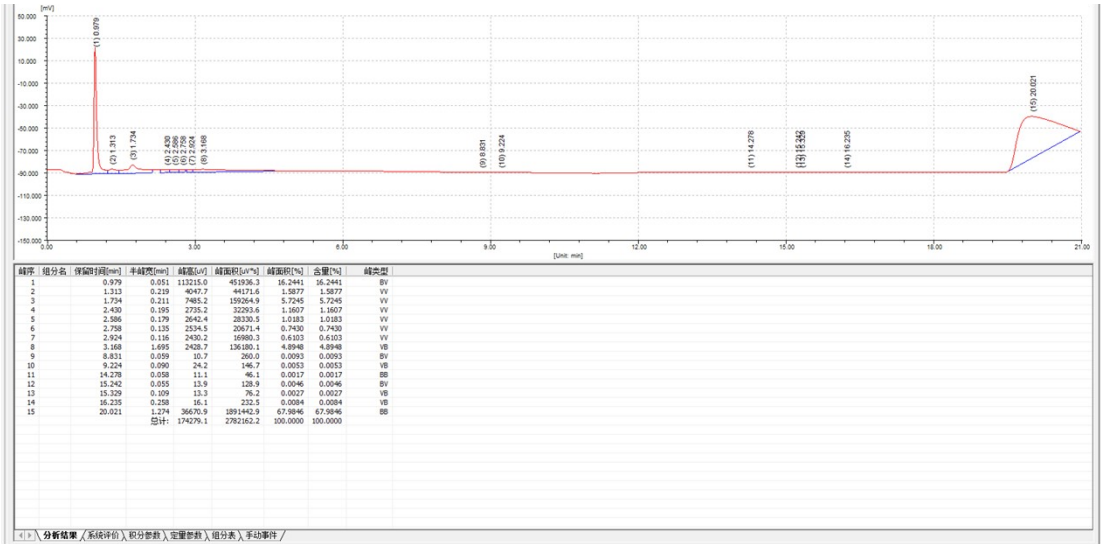

峰序	组分名	保留时间[min]	半峰宽[min]	峰高[uV]	峰面积[uV*s]	峰面积[%]	含量[%]	峰类型
1		0.979	0.051	113215.0	451936.3	16.2441	16.2441	BV
2		1.313	0.219	4047.7	44171.6	1.5877	1.5877	VV
3		1.734	0.211	7485.2	159264.9	5.7245	5.7245	VV
4		2.430	0.195	2735.2	32293.6	1.1607	1.1607	VV
5		2.586	0.179	2642.4	28330.5	1.0183	1.0183	VV
6		2.758	0.135	2534.5	20671.4	0.7430	0.7430	VV
7		2.924	0.116	2430.2	16980.3	0.6103	0.6103	VV
8		3.168	1.695	2428.7	136180.1	4.8948	4.8948	VB
9		8.831	0.059	10.7	260.0	0.0093	0.0093	BV
10		9.224	0.090	24.2	146.7	0.0053	0.0053	VB
11		14.278	0.058	11.1	46.1	0.0017	0.0017	BB
12		15.242	0.055	13.9	128.9	0.0046	0.0046	BV
13		15.329	0.109	13.3	76.2	0.0027	0.0027	VB
14		16.235	0.258	16.1	232.5	0.0084	0.0084	VB
15		20.021	1.274	36670.9	1891442.9	67.9846	67.9846	BB
		总计:		174279.1	2782162.2	100.0000	100.0000	

Fig. S14. The GC image of the reaction of Cu-C_3N_4-S with Ar as gas at −0.9 V vs. RHE. (H_2:~1min)

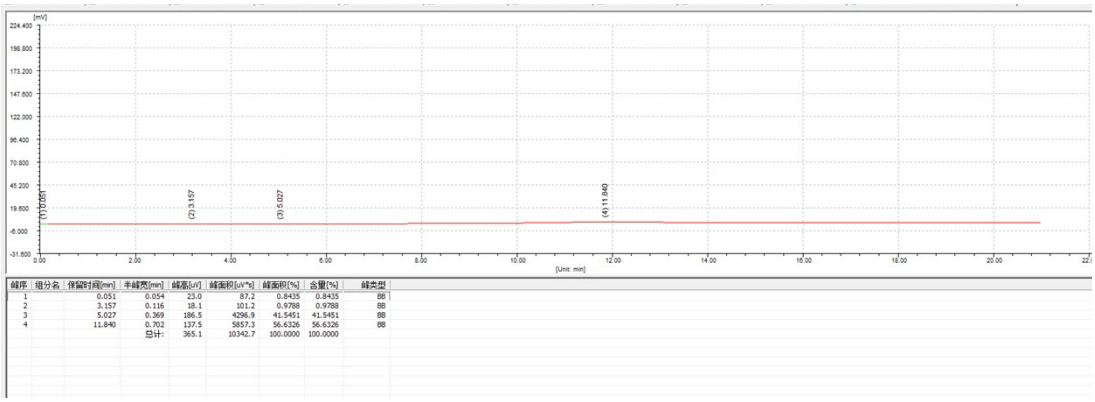

峰序	组分名	保留时间[min]	半峰宽[min]	峰高[uV]	峰面积[uV*s]	峰面积[%]	含量[%]	峰类型
1		0.051	0.054	23.0	87.2	0.8435	0.8435	BB
2		3.157	0.116	18.1	101.2	0.9788	0.9788	BB
3		5.027	0.369	186.5	4296.9	41.5451	41.5451	BB
4		11.840	0.702	137.5	5857.3	56.6326	56.6326	BB
			总计:	365.1	10342.7	100.0000	100.0000	

Fig. S15. The H_2 chromatogram of the reaction of Cu-C_3N_4-S with Ar as gas at -0.9 V vs. RHE.

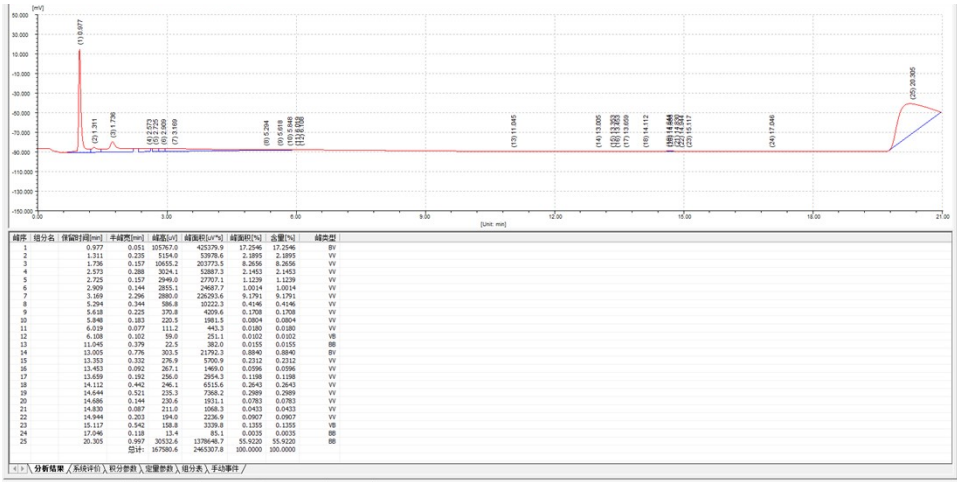

峰序	组分名	保留时间[min]	半峰宽[min]	峰高[uV]	峰面积[uV*s]	峰面积[%]	含量[%]	峰类型
1		0.977	0.051	105767.0	425379.9	17.2546	17.2546	BV
2		1.311	0.235	5154.0	53978.6	2.1895	2.1895	VV
3		1.736	0.157	10655.2	203773.5	8.2656	8.2656	VV
4		2.573	0.288	3024.1	52887.3	2.1453	2.1453	VV
5		2.725	0.157	2949.0	27707.1	1.1239	1.1239	VV
6		2.909	0.144	2855.1	24687.7	1.0014	1.0014	VV
7		3.169	2.296	2880.0	226293.6	9.1791	9.1791	VV
8		5.294	0.344	586.8	10222.3	0.4146	0.4146	VV
9		5.618	0.225	370.8	4209.6	0.1708	0.1708	VV
10		5.848	0.183	220.5	1981.5	0.0804	0.0804	VV
11		6.019	0.077	111.2	443.3	0.0180	0.0180	VV
12		6.108	0.102	59.0	251.1	0.0102	0.0102	VB
13		11.045	0.379	22.5	382.0	0.0155	0.0155	BB
14		13.005	0.776	303.5	21792.3	0.8840	0.8840	BV
15		13.353	0.332	276.9	5700.9	0.2312	0.2312	VV
16		13.453	0.092	267.1	1469.0	0.0596	0.0596	VV
17		13.659	0.192	256.0	2954.3	0.1198	0.1198	VV
18		14.112	0.442	246.1	6515.6	0.2643	0.2643	VV
19		14.644	0.521	235.3	7368.2	0.2989	0.2989	VV
20		14.686	0.144	230.6	1931.1	0.0783	0.0783	VV
21		14.830	0.087	211.0	1068.3	0.0433	0.0433	VV
22		14.944	0.203	194.0	2236.9	0.0907	0.0907	VV
23		15.117	0.542	158.8	3339.8	0.1355	0.1355	VB
24		17.046	0.118	13.4	85.1	0.0035	0.0035	BB
25		20.305	0.997	30532.6	1378648.7	55.9220	55.9220	BB
			总计:	167580.6	2465307.8	100.0000	100.0000	

Fig. S16. The GC image of the reaction of C_3N_4 with Ar as gas at -0.9 V vs. RHE.

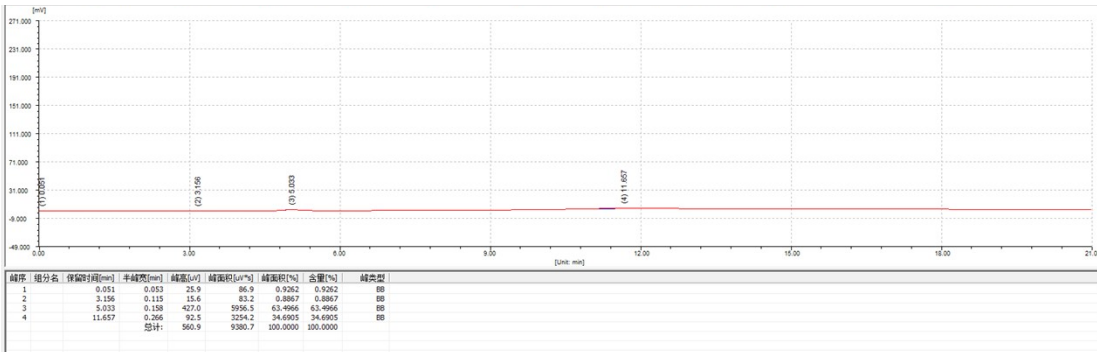

峰序	组分名	保留时间[min]	半峰宽[min]	峰高[uV]	峰面积[uV*s]	峰面积[%]	含量[%]	峰类型
1		0.051	0.053	25.9	86.9	0.9262	0.9262	BB
2		3.156	0.115	15.6	83.2	0.8867	0.8867	BB
3		5.033	0.158	427.0	5956.5	63.4966	63.4966	BB
4		11.657	0.266	92.5	3254.2	34.6905	34.6905	BB
			总计:	560.9	9380.7	100.0000	100.0000	

Fig. S17. The H_2 chromatogram of the reaction of C_3N_4 with Ar as gas at -0.9 V vs. RHE. (H_2:~1min)

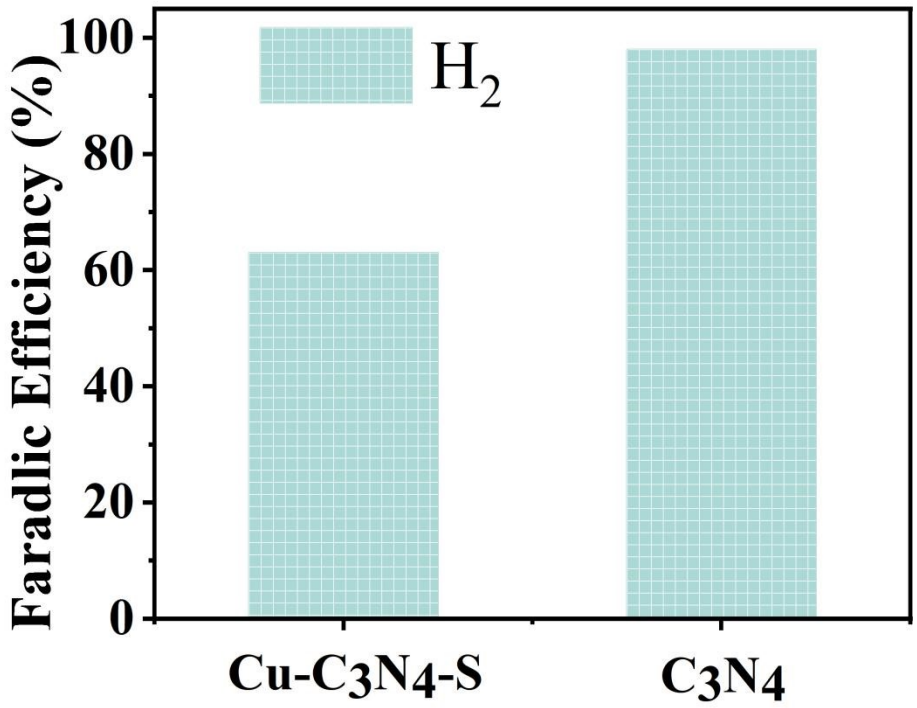

Fig. S18. The proportion of Cu-C_3N_4-S and C_3N_4 products with Ar as gas at the potential of -0.9 V vs. RHE.

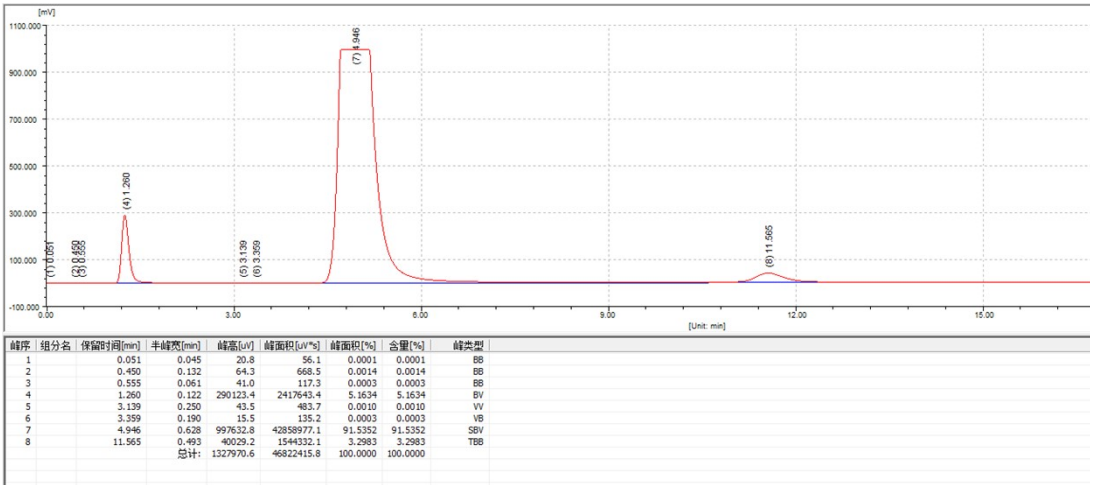

峰序	组分名	保留时间[min]	半峰宽[min]	峰高[uV]	峰面积[uV*s]	峰面积[%]	含量[%]	峰类型
1		0.051	0.045	20.8	56.1	0.0001	0.0001	BB
2		0.450	0.132	64.3	668.5	0.0014	0.0014	BB
3		0.555	0.061	41.0	117.3	0.0003	0.0003	BB
4		1.260	0.122	290123.4	2417643.4	5.1634	5.1634	BV
5		3.139	0.250	43.5	483.7	0.0010	0.0010	VV
6		3.359	0.190	15.5	135.2	0.0003	0.0003	VB
7		4.946	0.628	997632.8	42858977.1	91.5352	91.5352	SBV
8		11.565	0.493	40029.2	1544332.1	3.2983	3.2983	TBB
			总计:	1327970.6	46822415.8	100.0000	100.0000	

Fig. S19. The GC image of CO_2 reduction reaction for Cu−C_3N_4-S at −0.9 V vs. RHE. (CO: ~ 1.3 min, CH_4: ~2.6 min and C_2H_4: ~ 11 min)

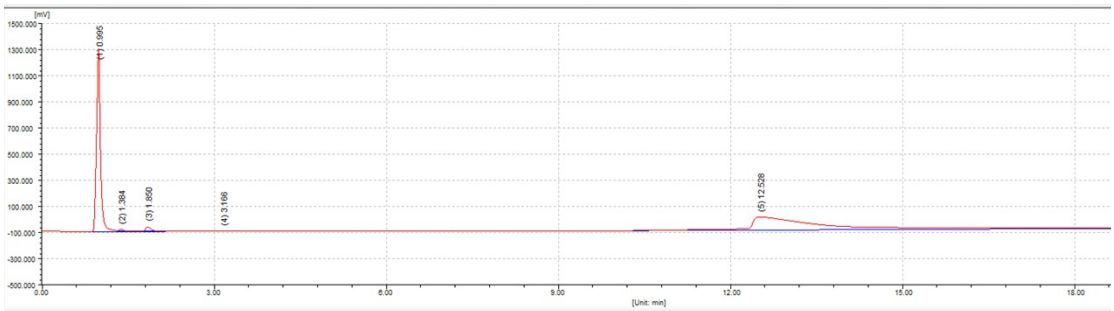

峰序	组分名	保留时间[min]	半峰宽[min]	峰高[uV]	峰面积[uV*s]	峰面积[%]	含量[%]	峰类型
1		0.995	0.066	1405214.1	6928770.4	38.9594	38.9594	SBV
2		1.384	0.067	12535.6	54055.3	0.3039	0.3039	TBB
3		1.850	0.105	33870.3	236489.9	1.3297	1.3297	TBB
4		3.166	0.177	207.8	4487.9	0.0252	0.0252	TBB
5		12.528	1.005	102200.4	10560805.7	59.3817	59.3817	BB
			总计:	1554028.1	17784609.4	100.0000	100.0000	

Fig. S20. The H_2 chromatograms of CO_2 reduction reaction for Cu−C_3N_4-S at −0.9 V vs. RHE. (H_2: ~ 1min)

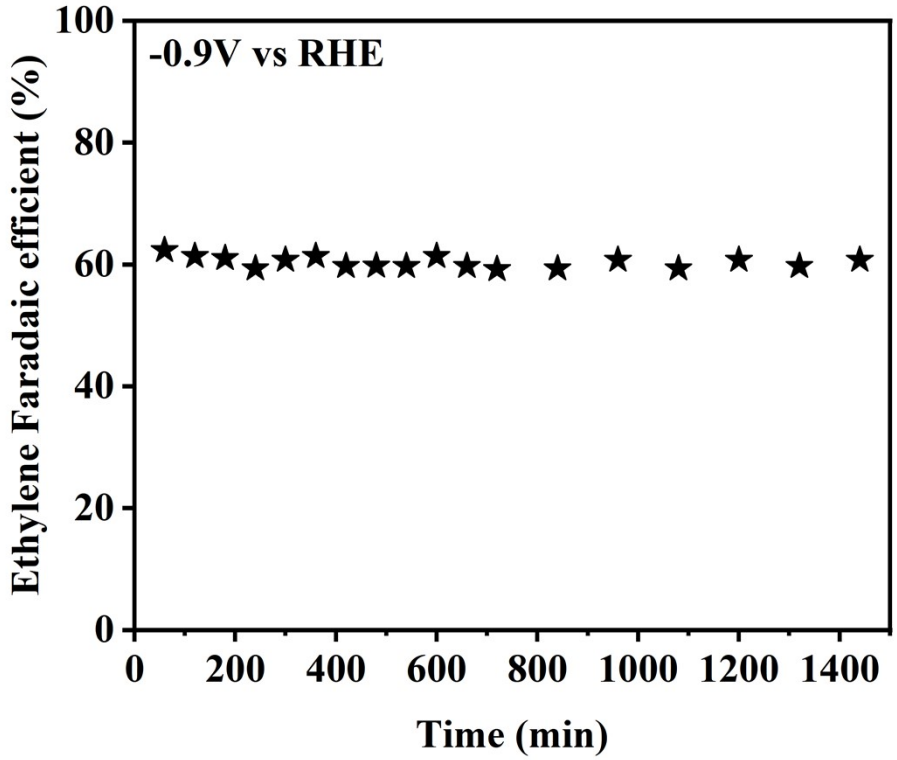

Fig. S21. Stability test for $Cu_{10\%}$-C_3N_4-S at −0.9 V vs. RHE with 1440 min of continuous.

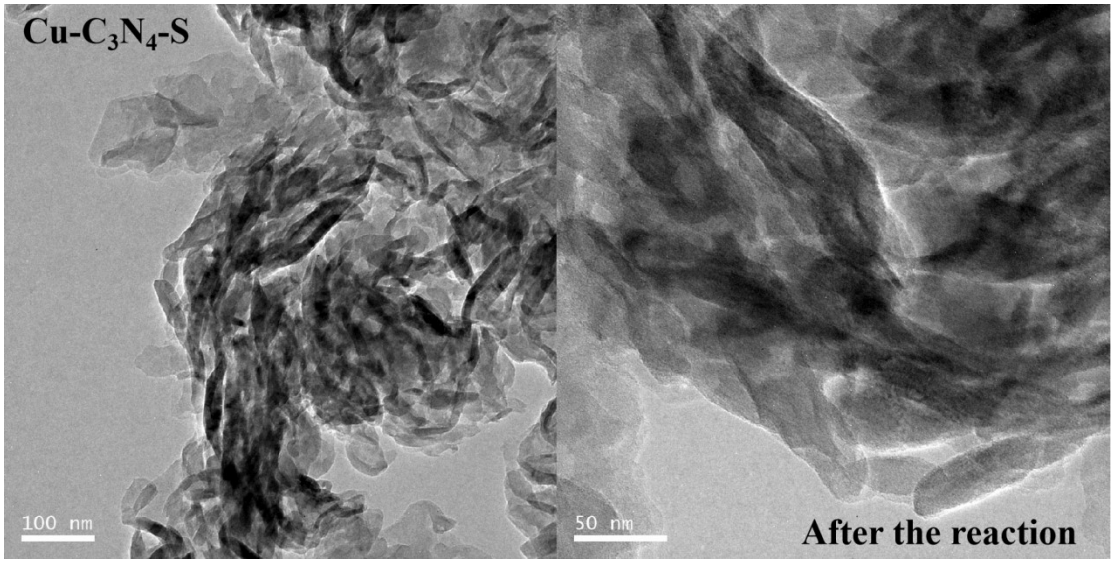

Fig.S22. HRTEM images of Cu-C_3N_4-S after the reaction.

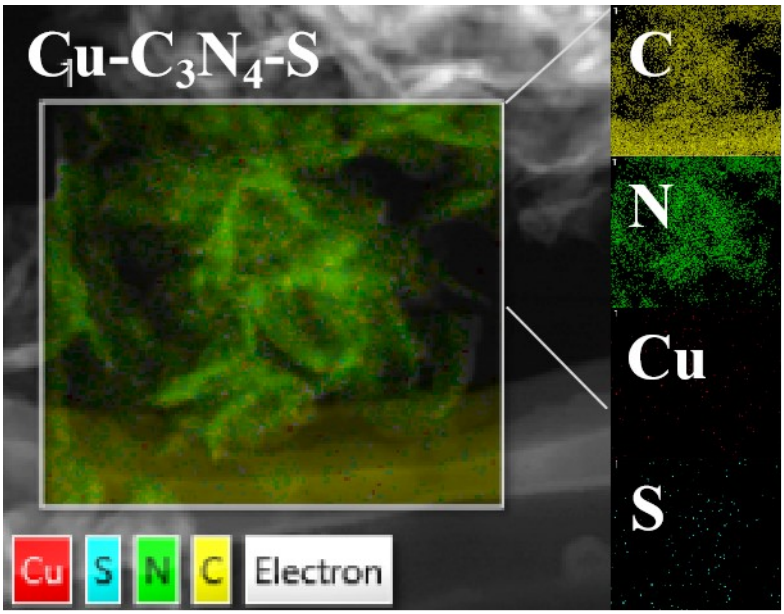

Fig.S23. HRTEM and corresponding EDX mapping images of Cu-C_3N_4-S after the reaction.

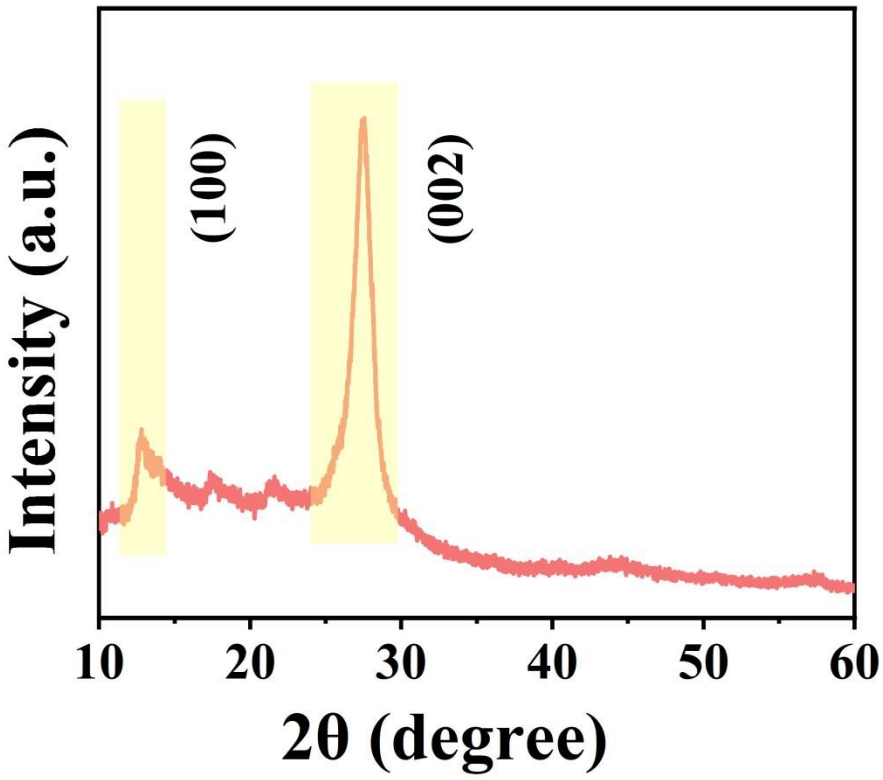

Fig. S24. XRD pattern of Cu-C_3N_4-S after the reaction.

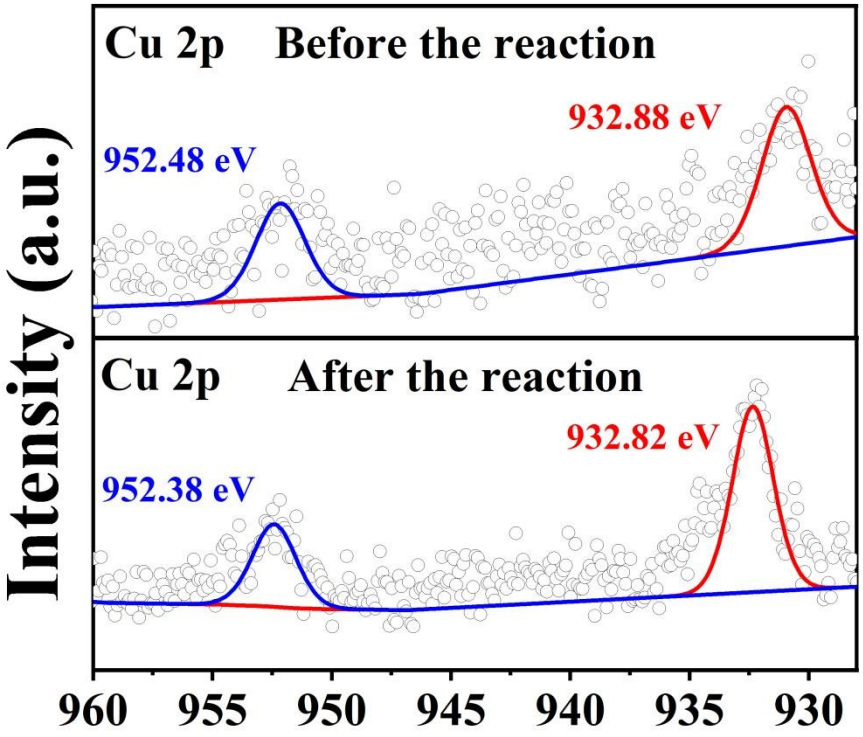

Fig. S25. High-resolution Cu 2p spectra of Cu-C_3N_4-S before and after the reaction.

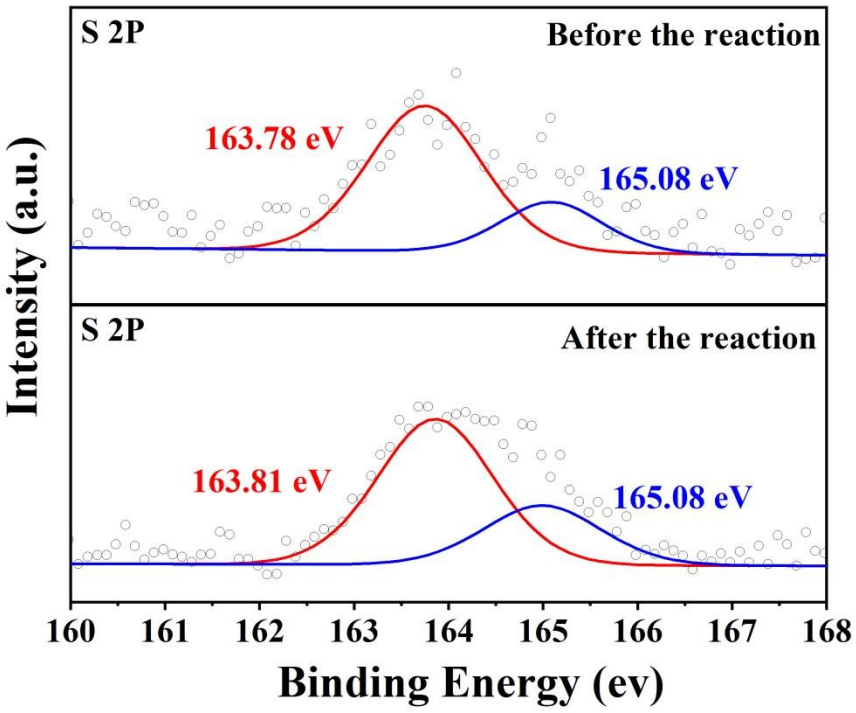

Fig.S26. High-resolution S 2p spectra of Cu-C_3N_4-S before and after the reaction.

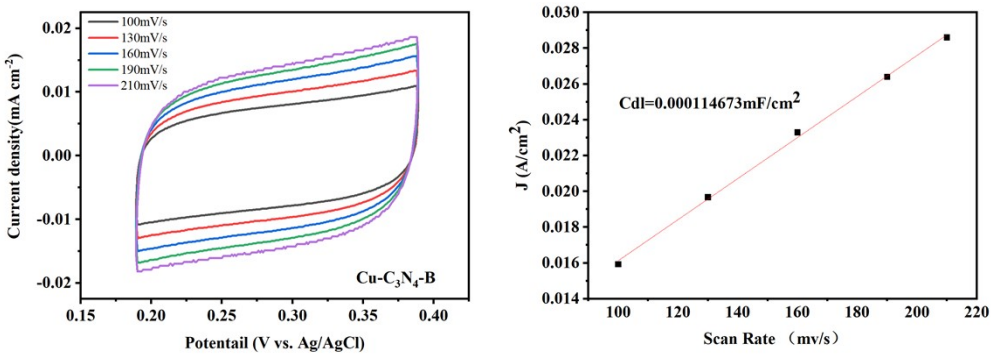

Fig. S27. The cyclic voltammograms measurements and the double-layer capacitance (C_{dl}) were conducted at various scan rates (100, 130, 160, 190, 210 mV s^{-1}) on Cu-C_3N_4-B.

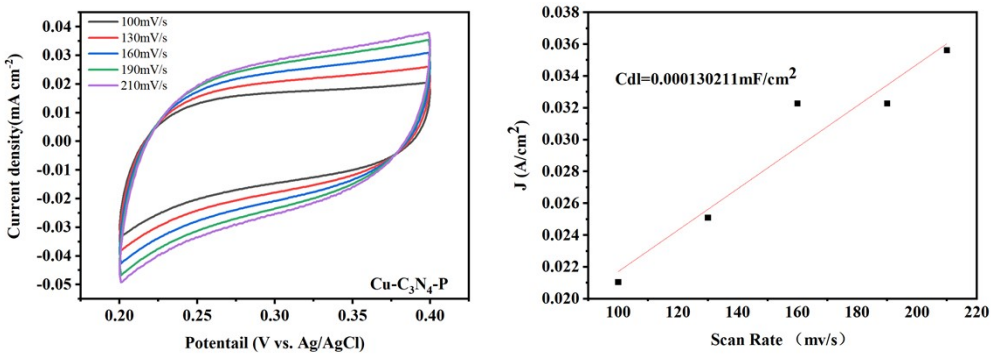

Fig. S28. The cyclic voltammograms measurements and the double-layer capacitance (C_{dl}) were conducted at various scan rates (100, 130, 160, 190, 210 mV s^{-1}) on Cu-C_3N_4-P.

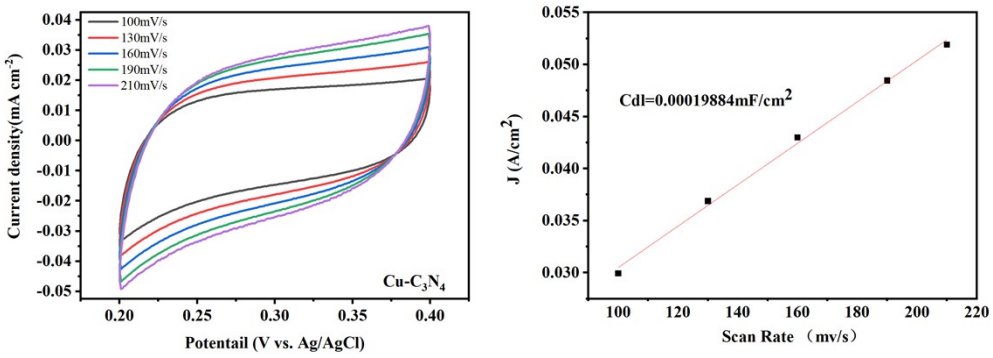

Fig. S29. The cyclic voltammograms measurements and the double-layer capacitance (C_{dl}) were conducted at various scan rates (100, 130, 160, 190, 210 mV s^{-1}) on Cu-C_3N_4.

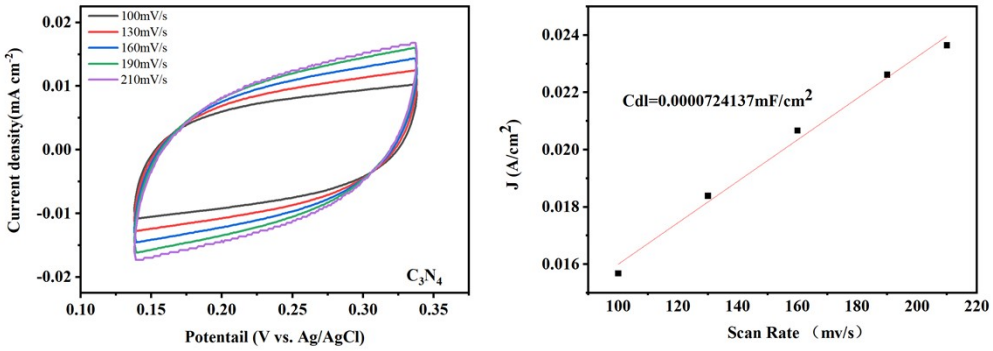

Fig. S30. The cyclic voltammograms measurements and the double-layer capacitance (C_{dl}) were conducted at various scan rates (100, 130, 160, 190, 210 mV s^{-1}) on C_3N_4.

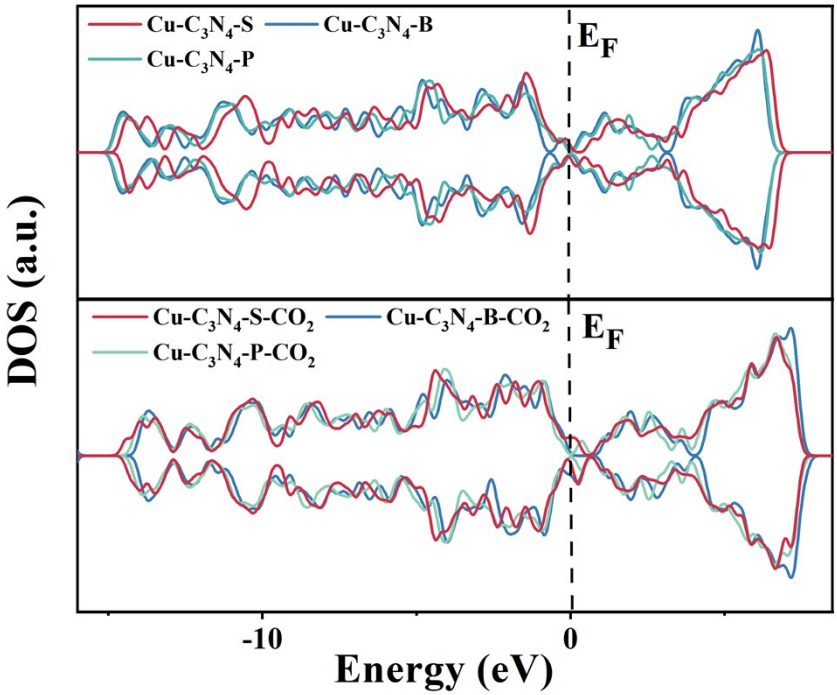

Fig. S31. The DOS of Cu-C_3N_4-HA before and after CO_2 absorption.

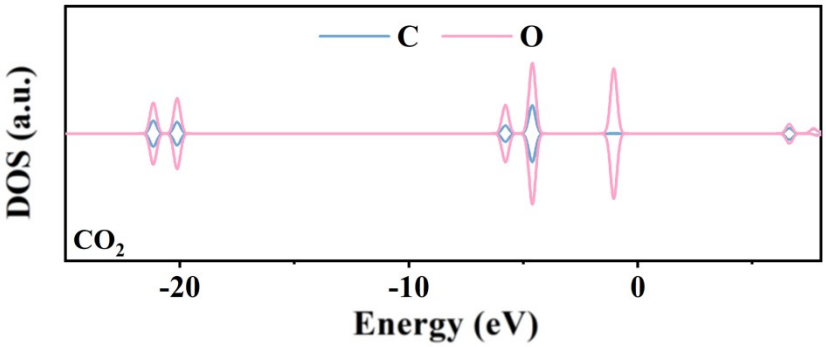

Fig. S32. The DOS of CO_2.

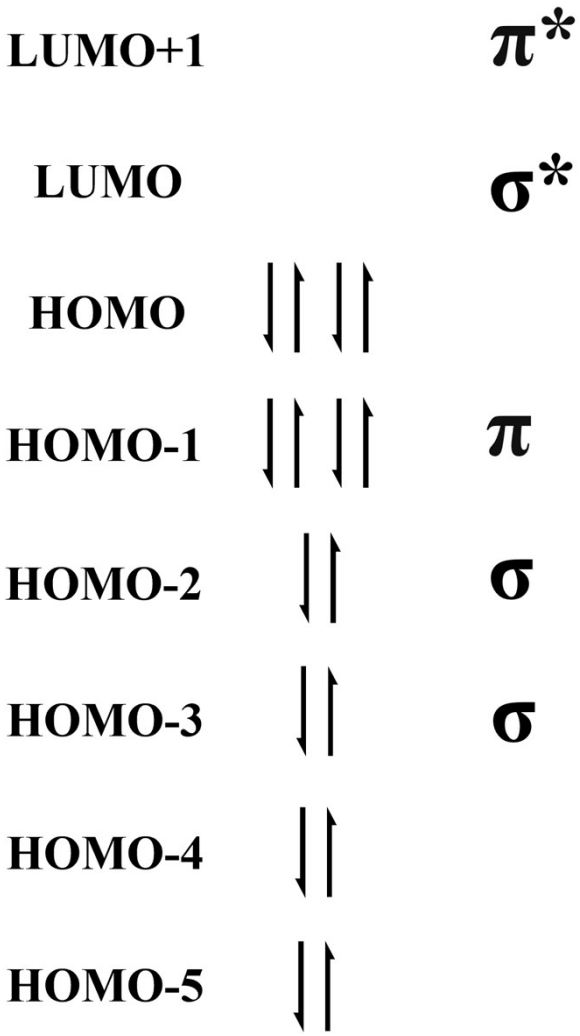

Fig. S33. The schematic representation of the molecular orbital diagram of CO_2.

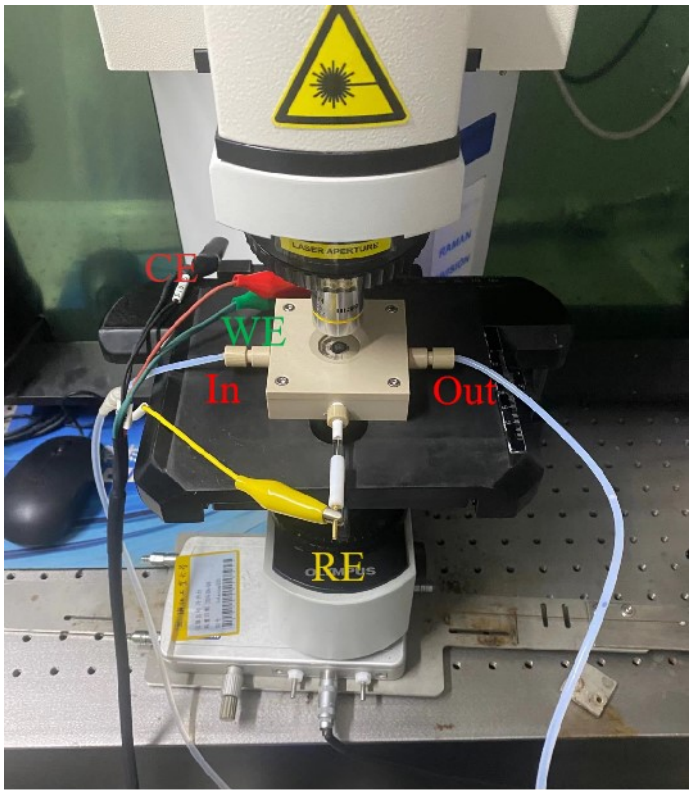

Fig. S34. Schematic representation of In-situ Raman device.

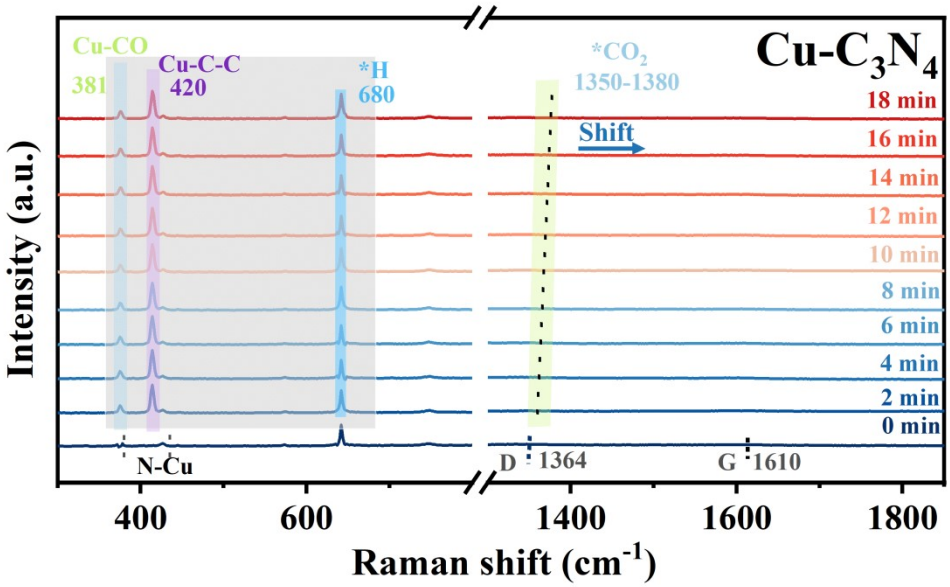

Fig. S35. Interval of 2 minutes in-situ Raman spectra under CO_2RR conditions of Cu-C_3N_4 from 300 to 1850 cm^{-1}.

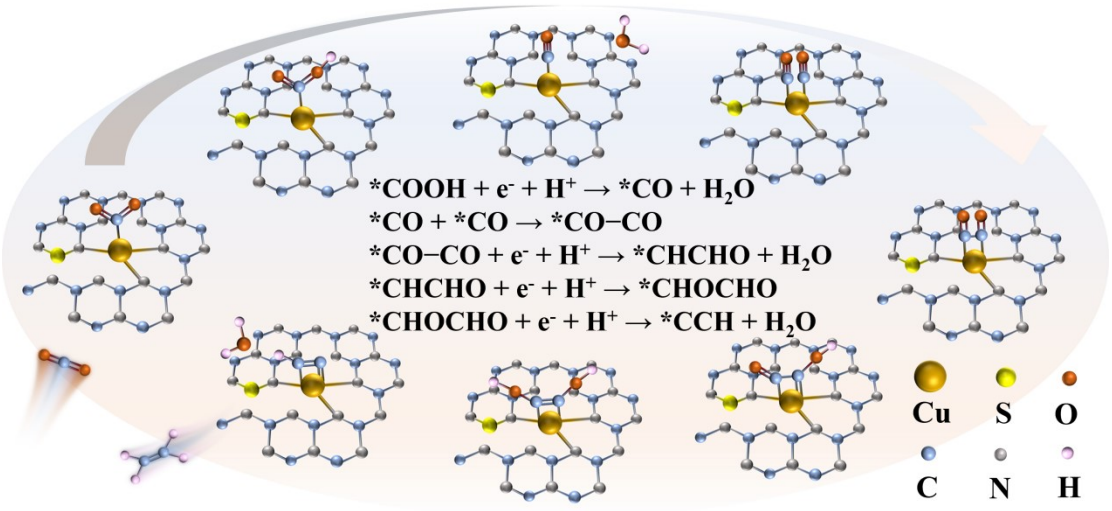

Fig. S36. Potential pathway of Cu-C_3N_4-S for the reduction of CO_2 to C_2H_4.

Table S1.: Concentrations of non-metallic elements in different Cu-C_3N_4-HA samples

Catalyst	S (%)	B (%)	P (%)
Cu-C_3N_4-S	4.4	-	-
Cu-C_3N_4-B	-	4.2	-
Cu-C_3N_4-P	-	-	2.8

Table S2. Fitted parameters of the Cu-C_3N_4-S.

Sample	Path	N[a]	R (Å)[b]	σ^2 (10^{-3}Å^2)[c]	ΔE_0 (eV)[d]	R-factor[e]
Cu-C_3N_4-S	Cu-N	3.02	2.01	6.41	2.14	0.019

[a]N, coordination number; [b]R, distance between absorber and backscatter atoms; [c]σ^2, Debye-Waller factor to account for both thermal and structural disorders; [d]ΔE_0, inner potential correction; [e]R factor indicates the goodness of the fit.

Table S3. Comparison of the electroreduction CO_2 to C_2H_4 performance for various catalysts.

Catalyst	FE_{C2H4} (%)	Potential (V vs. RHE)	Reference
Cu-C_3N_4-S	**60.2**	**-0.9**	**This Work**
Cu/$HMCS_5$-10%	68.6	-1	[8]
Cu–MOF–CF	48.6	-1.11	[9]
Pd-Cu_2O	63.8	-1.1	[10]
P-Cu-2	48.6	-1.09	[11]
60-CuO/CeO_2	44.8	-1.27	[12]
Cu-KBr	52	-1.1	[13]
OBC	45	-1	[14]
La_2CuO_4 NBs	60	-1	[15]
PTF(Ni)/Cu	57.3	-1.1	[16]
Cu/CuxSy	60	-1.32	[17]
Cu_3N NCs	60	-1.6	[18]
Cu-based NP/C	57.3	-1.1	[19]
PcCu-Cu-O	50	-1.2	[20]
CuPANI	40	-1.2	[21]
Ag_{65}-Cu_{35}JNS-100	54	-1.2	[22]

References

[1] G. Kresse, J. Hafner, Ab initio molecular dynamics for liquid metals, Phys. Rev. B 47 (1993) 558-561.

[2] G. Kresse, J. Hafner, Ab initio molecular-dynamics simulation of the liquid-metal-amorphous-semiconductor transition in germanium, Phys. Rev. B 49 (1994) 14251-14269.

[3] J. P. Perdew, K. Burke, M. Ernzerhof, Generalized gradient approximation made simple. Phys. Rev. Lett. 77 (1996) 3865-3868.

[4] G. Kresse, D. Joubert, Form ultrasoft pseudopotentials to the projector augmented-wave method. Phys. Rev. B 59 (1999) 1758-1775.

[5] P.E. Blochl, Projector augmented-wave method, Phys Rev B Condens Matter 50 (1994) 17953-17979.

[6] Nørskov JK, Rossmeisl J, Logadottir A, Lindqvist L, Kitchin JR, Bligaard T, Jonsson H. Origin of the overpotential for oxygen reduction at a fuel-cell cathode. J. Phys. Chem. B 108 (2004) 17886–17892.

[7] Bendavid LI, Carter EA. CO_2 Adsorption on Cu_2O (111): A DFT+U and DFT-D study, J. Phys. Chem. C 117 (2013), 26048–26059.

[8] D.H. Nam, O. Shekhah, A. Ozden, C. McCallum, F. Li, X. Wang, Y. Lum, T. Lee, J. Li, J. Wicks, A. Johnston, D. Sinton, M. Eddaoudi, E.H. Sargent, High-rate and selective CO_2 electrolysis to ethylene via meta-organic-framework-augmented CO_2 availability, Adv. Mater. 34 (2022) 2207088.

[9] T. Yan, P. Wang,W.Y. Sun, Single-site netal-organic framework and copper foil tandem catalyst for highly selective CO_2 electroreduction to C_2H_4, Small 19 (2022) 2206070.

[10] D. Xiao, X. Bao, M. Zhang, Z. Li, Z. Wang, Y. Gao, Z. Zheng, P. Wang, H. Cheng, Y. Liu, Y. Dai, B. Huang, Stabilizing Cu_2O for enhancing selectivity of CO_2 electroreduction to C_2H_4 with the modification of Pd nanoparticles, Chem. Eng. J. 45 (2023) 139358.

[11] J. Zhang, Z. Liu, H. Guo, H. Lin, H. Wang, X. Liang, H. Hu, Q. Xia, X. Zou, X. Huang, Selective, Stable Production of ethylene using a pulsed Cu-Based electrode, ACS Appl. Mater. Inter. 14 (2022) 19388-19396.

[12] H.-D. Cai, B. Nie, P. Guan, Y.-S. Cheng, X.-D. Xu, F.-H. Wu, G. Yuan, X.-W. Wei, Tuning the interactions in CuO nanosheet-decorated CeO_2 nanorods for controlling the electrochemical reduction of CO_2 to methane or ethylene, ACS Appl. Nano Mater. 55 (2022) 7259-7267.

[13] T. Kim, G.T.R. Palmore, A scalable method for preparing Cu electrocatalysts that convert CO_2 into C_{2+} products, Nat. Commun. 111 (2020) 3622.

[14] W. Zhang, C. Huang, Q. Xiao, L. Yu, L. Shuai, P. An, J. Zhang, M. Qiu, Z. Ren, Y. Yu, Atypical oxygen-bearing copper boosts ethylene selectivity toward electrocatalytic CO_2 Reduction, J Am Chem Soc 142 (2020) 11417-11427.

[15] J. Wang, C. Cheng, B. Huang, J. Cao, L. Li, Q. Shao, L. Zhang, X. Huang, Grain-Boundary-Engineered La_2CuO_4 Perovskite nanobamboos for efficient CO_2 reduction reaction, Nano Lett. 212 (2021) 980-987.

[16] D.L. Meng, M.D. Zhang, D.H. Si, M.J. Mao, Y. Hou, Y.B. Huang, R. Cao, Highly selective tandem electroreduction of CO_2 to ethylene over atomically isolated nickel-nitrogen site/copper nanoparticle

catalysts, Angew. Chem. Int. Ed. 60 (2021) 25485-25492.
[17] C.F. Wen, M. Zhou, P.F. Liu, Y. Liu, X. Wu, F. Mao, S. Dai, B. Xu, X.L. Wang, Z. Jiang, P. Hu, S. Yang, H.F. Wang, H.G. Yang, Highly ethylene-selective electrocatalytic CO_2 reduction enabled by isolated Cu-S motifs in metal-organic framework based precatalysts, Angew. Chem. Int. Ed. 61 (2021) 25485-25492.
[18] Z. Yin, C. Yu, Z. Zhao, X. Guo, M. Shen, N. Li, M. Muzzio, J. Li, H. Liu, H. Lin, J. Yin, G. Lu, D. Su, S. Sun, Cu_3N nanocubes for selective electrochemical reduction of CO_2 to rthylene, Nano Lett. 19 (2019) 8658-8663.
[19] H. Jung, S.Y. Lee, C.W. Lee, M.K. Cho, D.H. Won, C. Kim, H.S. Oh, B.K. Min, Y.J. Hwang, Electrochemical fragmentation of Cu_2O nanoparticles enhancing selective C-C coupling from CO_2 reduction reaction, J. Am. Chem. Soc. 141 (2019) 4624-4633.
[20] X.-F. Qiu, H.-L. Zhu, J.-R. Huang, P.-Q. Liao, X.-M. Chen, Highly selective CO_2 electroreduction to C_2H_4 using a metal-organic framework with dual active sites, J. Am. Chem. Soc. 143 (2021) 7242-7246.
[21] X. Wei, Z. Yin, K. Lyu, Z. Li, J. Gong, G. Wang, L. Xiao, J. Lu, L. Zhuang, Highly delective teduction of CO_2 to C_{2+} hydrocarbons at copper/polyaniline interfaces, ACS Catal. 107 (2020) 4103-4111.
[22] Y. Ma, J. Yu, M. Sun, B. Chen, X. Zhou, C. Ye, Z. Guan, W. Guo, G. Wang, S. Lu, D. Xia, Y. Wang, Z. He, L. Zheng, Q. Yun, L. Wang, J. Zhou, P. Lu, J. Yin, Y. Zhao, Z. Luo, L. Zhai, L. Liao, Z. Zhu, R. Ye, Y. Chen, Y. Lu, S. Xi, B. Huang, C.S. Lee, Z. Fan, Confined growth of silver-copper janus nanostructures with {100} facets for highly selective tandem electrocatalytic carbon dioxide reduction, Adv. Mater. 34 (2022) 2110607.